Applied Thermal Engineering 111 (2017) 377–386

Contents lists available at ScienceDirect

Applied Thermal Engineering

journal homepage: www.elsevier.com/locate/apthermeng

Research Paper

Application of Peltier thermal diodes in a magnetocaloric heat pump

Wouter de Vries *, Theo H. van der Meer

University of Twente, Faculty of Engineering Technology, Department of Thermal Engineering, Drienerlolaan 5, 7522 NB Enschede, The Netherlands

HIGHLIGHTS

- A 2D model including the thermoelectric and magnetocaloric effect is developed.
- Diode thermal resistance is based on commercially available Peltier modules.
- The temperature and heat flux behavior of the device is presented.
- Operational and geometric parameter permutations are investigated.
- Superior device performance is observed without the magnetocaloric effect.

ARTICLE INFO

Article history:
Received 15 July 2016
Revised 12 September 2016
Accepted 19 September 2016
Available online 21 September 2016

Keywords:
Magnetic refrigeration
Magnetocaloric effect
Thermal diodes
Peltier modules
Microchannel heat exchangers
Heat transfer

ABSTRACT

The major hurdle for commercialization of room temperature magnetic refrigeration is the inadequate power density of a device due to the low operating frequency. Limitation in the heat transfer rate imposed by solid-fluid convection is the primary cause. Applying Peltier thermal diodes in combination with microchannel heat exchangers has been investigated as a possible solution. This study improves in realism upon earlier work, mainly by extending the calculations with a modeled thermoelectric effect.

After reverse engineering the Micropelt MPC-D701 Peltier module, behavior of a 2D single-stage device is examined, consisting of two Peltier modules with heat exchangers enveloping a thin layer of magnetocaloric material. The near optimal switching frequency is determined and performance characteristics are calculated for several configurations of varying load, field strength and fluid velocity. A better performance is observed without the magnetocaloric effect due to reduced heat leakage through the passive thermal diode. This behavior extends to multiple devices in series where active magnetic regeneration is induced. Two possible solutions were explored, but these did not show significant improvement in device performance when applying the magnetocaloric effect.

1. Introduction

Room temperature magnetic refrigeration is a promising alternative to vapor-compression technology. A major advantage is the absence of a hazardous refrigerant. The working principle is based on the Magneto-Caloric Effect (MCE) induced by magnetization and demagnetization of a Magneto-Caloric Material (MCM). For practical applications Active Magnetic Regeneration (AMR) is applied to reach the required temperature span. Ample explanation of the MCE and possible AMR implementations is given in the book written by Kitanovski et al. [1].

A recurring topic is the improvements needed for commercialization of magnetic refrigeration. Prevalent attention is given to the power density, defined as cooling power per kilogram MCM. This metric is structurally too small for prototypes at efficient operating conditions. Consequently, large amounts of magnetocaloric material are needed, yielding a big magnetized volume and resulting permanent magnet mass. Both device cost and environmental impact remain subpar for as long as no improvement is made.

The operating frequency or number of thermodynamic cycles per unit time of a device is directly proportional to its power density. Performance of conventional AMR implementations degrades at high frequencies due to convective heat transfer limitations between the MCM and transport fluid. Either the MCE is not fully exploited by lack of heat exchanged or the pressure work to overcome fluid resistance becomes unreasonably high due to the low permeability.

An alternative to convective heat transfer between the MCM and the fluid, employing solid-state thermal diodes, was proposed by Kitanovski and Egolf [2]. Further investigation is carried out by Silva [3,4], Olsen [5], Tomc [6,7] and Egolf himself [8]. Their

* Corresponding author.
E-mail address: wdevries@outlook.com (W. de Vries).

http://dx.doi.org/10.1016/j.applthermaleng.2016.09.103
1359-4311/

Nomenclature

Standard

a_{sf}	specific surface area (m^{-1})
b	channel width (m)
C_p	heat capacity ($J\,kg^{-1}\,K^{-1}$)
D	channel or fin height (m)
$\vec{E}$	electric field ($V\,m^{-1}$)
D_h	hydraulic diameter (m)
d_z	depth (m)
H	applied magnetic field (T)
h_{sf}	heat transfer coefficient ($W\,m^{-2}\,K^{-1}$)
$\vec{I}$	current (A)
$\vec{J}$	current density ($A\,m^{-2}$)
k	thermal conductivity ($W\,m^{-2}\,K$)
M	specific magnetization ($A\,m^2\,kg^{-1}$)
$\dot{m}$	mass flow ($kg\,s^{-1}$)
N_{ch}	number of channels
$\vec{n}$	normal vector
P	Peltier coefficient (V)
P_{el}	electric input power (W)
$\dot{Q}_{c,load}$	cooling power (W)
$\dot{Q}_h$	heating power (W)
$\dot{Q}_{MCE}$	magnetocaloric effect ($W\,m^{-3}$)
S	Seebeck coefficient ($V\,K^{-1}$)
T	temperature (K)
t	time (s)
$\vec{U}$	velocity ($m\,s^{-1}$)
$\vec{u}_f$	microchannel velocity ($m\,s^{-1}$)
$\vec{u}_p$	porous medium velocity ($m\,s^{-1}$)
V	electric potential (V)
W	device width (m)
$\dot{W}_{mag}$	magnetic work input (W)
w	channel wall or fin thickness (m)

Greek

α	thermal diffusivity ($m^2\,s^{-1}$)
η_{fin}	fin efficiency
θ_p	solid volume fraction
ρ	density, $kg\,m^{-3}$
σ	electrical conductivity, $s\,m^{-1}$
τ_{cycle}	cycle or period length (s)

Sub- and superscripts

f	fluid
s	solid
c	cold
h	hot
overline	time average over cycle or period

Acronyms

AMR	Active Magnetic Regenerat(ion/or)
CHEX	Cold Heat Exchanger
COP	Coefficient Of Performance
HHEX	Hot Heat Exchanger
MCE	Magneto-Caloric Effect
MCM	Magneto-Caloric Material

conclusion is unanimously positive and further research is recommended. Tomc [6] has created the most elaborate model thus far when focusing on thermoelectric thermal diodes based on the Peltier effect. In this article, the level of detail and realism are further improved by adding a model for the thermoelectric effect and going from quasi 2D to full 2D by incorporating the heat exchangers.

Starting from a 3D implementation of a Peltier module in COMSOL Multiphysics 5.2, the conversion is made to 2D resulting in a single-stage device by including MCM and microchannel heat exchangers. After investigating the displayed behavior for different configurations with and without the MCE, multiple devices in series are simulated to induce regeneration. In the end, some options are explored to improve the device performance.

2. Investigated system

The investigated system is similar to the work of Tomc [6], as shown in Fig. 1a. A thin sheet of MCM is surrounded by Peltier modules or Peltier thermal diodes. Each layer of thermal diodes faces a microchannel heat exchanger where a heat transfer fluid, water in this case, flows through. By convention, the top heat exchanger contains the hot fluid (HHEX) and the bottom one the cold fluid (CHEX). Each fluid stream passes through an external heat exchanger where heat is either absorbed or released. AMR, similar to a conventional magnetocaloric heat pump, is achieved by using a single heat transfer fluid and routing CHEX outlet to HHEX inlet, as shown in Fig. 1b.

Besides a temperature difference in y-direction between CHEX and HHEX, a temperature gradient along the length of the device (x-direction) is induced by MCM regeneration. In theory, any temperature span (the delta in inlet temperatures) can be reached by increasing the device length and fine-tuning the Curie temperature of the MCM.

Tomc [6] used two fluid loops in his system, e.g. the outlets of CHEX and HHEX come back to their respective inlets. A direct consequence is that the maximum temperature span is limited to the ΔT between the hot and cold fluid, no active regeneration takes place. Heat leakage from hot to cold fluid causes a disastrous device efficiency reduction for high temperature spans. Tomc has underpredicted this effect by overestimating the diode thermal resistance ($97.7\,K\,W^{-1}$ instead of $7.3\,K\,W^{-1}$)[1]. He also assumed discontinuous water flow, which disregards one of the major advantages of this concept compared to a conventional AMR. For the system investigated here, the diode thermal resistance is predicted with higher accuracy by modeling the full geometry. Besides continuous instead of intermittent fluid flow is used.

2.1. Single-stage and basic operation

A slice of the system, indicated in Fig. 1a, consisting of a single Peltier module or thermal diode in x-direction, is named a single-stage device (similar to the terminology used by Kitanovski et al. [1]). In general, no regeneration takes place and the temperature gradients in x- and y-direction are of the same order of magnitude. The thermodynamic cycle starts from the moment just after magnetization where the MCM is heated by the MCE. The hot side thermal diode is enabled and rapidly transports heat from the MCM to HHEX in conjunction with conventional lattice conduction. The cold side thermal diode is passive but clearly some heat still leaks away to CHEX. Ideally, the magnetic field is removed when the

[1] A 1 mm thick layer of bismuth telluride with $k = 1\,W\,m^{-1}\,K^{-1}$ over an area of $10.24\,mm^2$ yields $97.7\,K\,W^{-1}$. The data sheet of the Peltier module [9] reports $7.3\,K\,W^{-1}$.

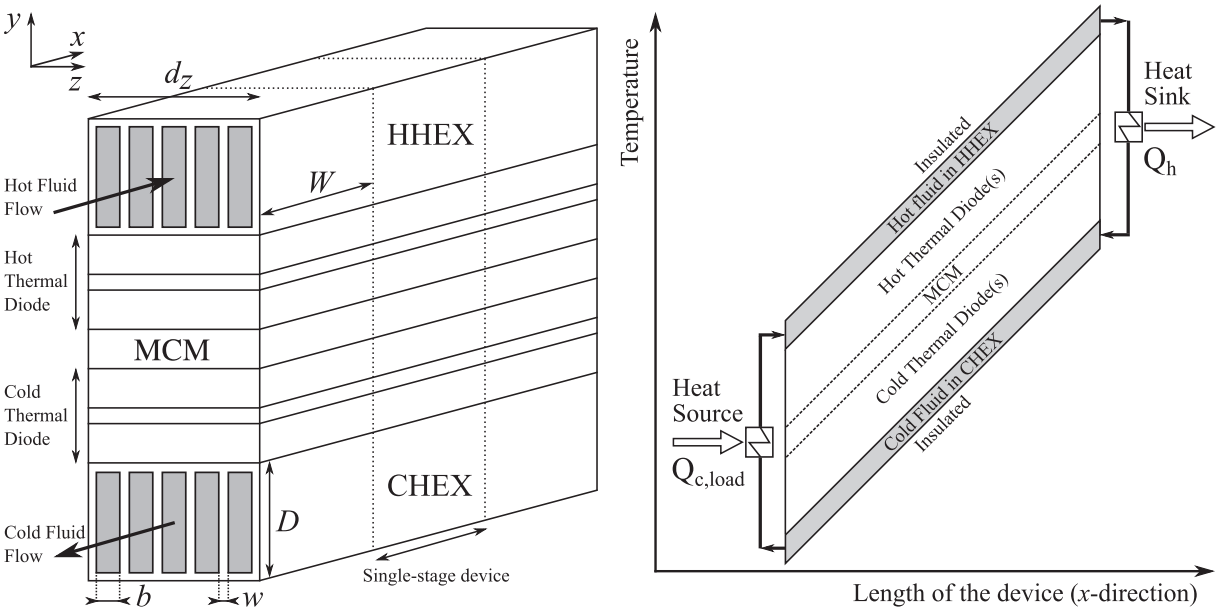

(a) System outline. The fluid channels are indicated in gray and the thermal diodes are implemented as Peltier modules.

(b) Expected temperature distribution over the length of device shown in figure 1a.

Fig. 1. Investigated system.

average hot side Peltier temperature drops below the hot fluid temperature. Continuing beyond this point reduces the Peltier module efficiency since temperature driven lattice conduction starts to counteract the heat transported by the Peltier effect. After demagnetization, where the MCE lowers the MCM temperature, the reverse process takes place; the cold side Peltier module transports heat from CHEX to the MCM until its average temperature rises above that of the cold side fluid. Simultaneously, the hot side thermal diode is passive and acts like an imperfect insulator.

2.2. Peltier thermal diode: Micropelt MPC-D701

The choice was made to use the same commercially available Peltier modules as Tomc [6] used in his paper: the Micropelt MPC-D701 (shown in Fig. 2). This is a thin film Peltier module which means it has a relatively high Coefficient of Performance (COP) and a fast response time to changes in electric current and temperature.

With the information given in the data sheet as provided by Micropelt, the best possible approximation with respect to geometry and performance has been made. All major dimensions are found in the schematic of Fig. 2b with exception of the thickness (1090 μm), which is mentioned on the Micropelt website[2]. The MPC-D701 module was reverse engineered using the data sheet [9] and papers published by Böttner [10–12].

The general topology is derived from Fig. 2c. Based on the scale, 6 legs fit next to each other, each approximately 500 μm in length and 50 μm in width. It is an even number since the contacts are on the same side. The module works by applying a current through an N-type leg – electrode – P-type leg – electrode and so on. The image shows the shape of the electrodes (rectangles isolated from each other) and either P- or N-type legs with solder applied. The other half of the module is manufactured in the same way with the electrodes shifted by half their height. The preferred electric current path is created when placed on top of each other and soldered together as shown in Fig. 3b.

[2] http://micropelt.com/products/mypelt.php, consulted on 16th of May 2016.

The total thickness of two electrodes and a leg with solder is 40 μm (1090 μm − 2 × 525 μm, from Fig. 2b). Using Fig. 2d the thickness of the electrode and solder are estimated to be 2.5 μm and 2 μm, which leaves 33 μm for the thermoelectric legs. The legs are made of N-type or P-type bismuth telluride on a silicon substrate (Fig. 2b). The electrodes and solder were assumed to be made of respectively gold and a lead-free tin-silver-copper alloy. Table 1 gives an overview of the materials used and their properties at 293.15 K. Temperature dependent properties were used where applicable.

2.3. Magnetocaloric material: Gadolinium

The most common near room temperature MCM is Gadolinium (Gd) with a Curie temperature of 293 K, which is therefore used in the current study. Magnetization and heat capacity data was obtained from Dan'kov [13]. The remaining properties were available in the COMSOL Multiphysics material library, see Table 1.

3. Methodology

This section describes the physics involved for each component of the magnetocaloric heat pump with Peltier thermal diodes. The device was studied in 2D (x, y-plane) to save computational time, although the Peltier module was analyzed in 3D to recursively determine actual geometry and material properties.

3.1. Magnetocaloric material

The time-dependent energy equation is solved for the MCM:

$$\rho C_p \frac{\partial T}{\partial t} + \vec{\nabla} \cdot (k \vec{\nabla} T) = \dot{Q}_{MCE} \tag{1}$$

where the magnetocaloric effect is modeled as a heat source:

$$\dot{Q}_{MCE} = -\rho T \frac{dH}{dt} \frac{\partial M(H,T)}{\partial T} \tag{2}$$

(a) Photo from the data sheet [9]

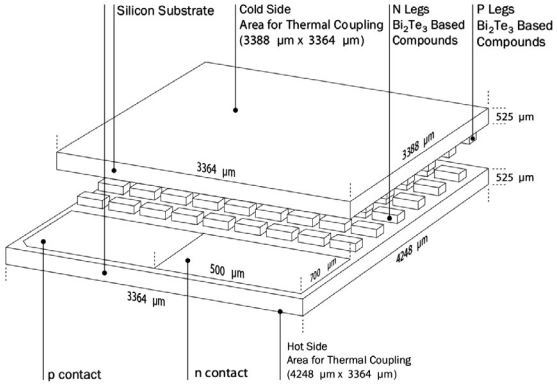

(b) Schematic from the data sheet [9]

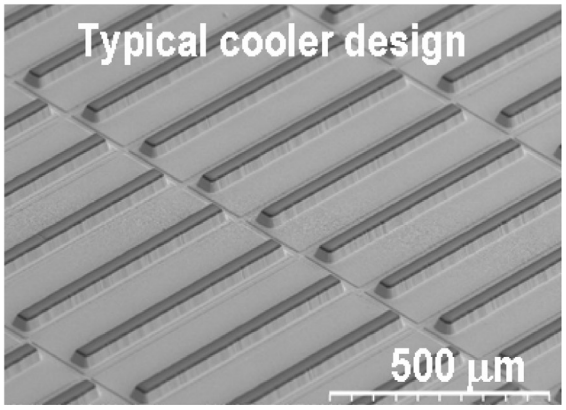

(c) Internal geometry overview,figure 3 of Böttner [12]

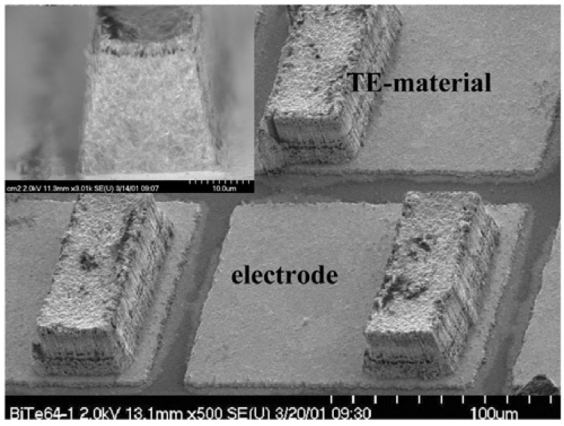

(d) Internal geometry closeup, figure 7 of Böttner [10]

Fig. 2. Micropelt MPC-D701.

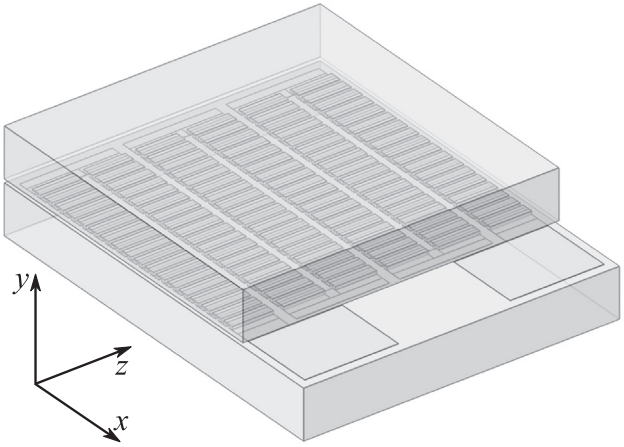

(a) Isometric view

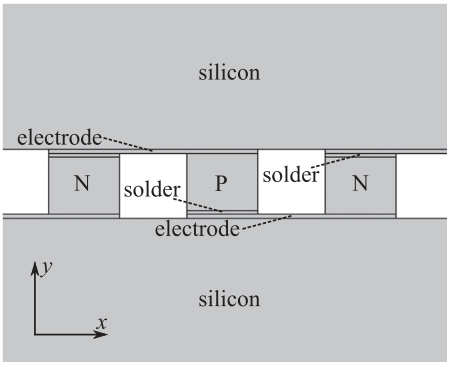

(b) Side view showing the different layers

Fig. 3. Micropelt MPC-D701 model.

Here, $H(t)$ is the applied magnetic field profile, which is assumed to be spatially uniform over the MCM and continuous in first and second derivative with respect to time. Magnetization and demagnetization are uniformly spaced at $0.25\tau_{cycle}$ and $0.75\tau_{cycle}$. The cycle or period length τ_{cycle} is inversely proportional to the operating frequency of the device. The magnetization time; the time required

Table 1
Material properties (with source when unavailable in COMSOL Multiphysics) and typical values at 293.15 K.

		Bi_2Te_3	Au	Sn-3.8Ag-0.7Cu	Si	Gd	H_2O
σ	($S\,m^{-1}$)	5.9×10^4 [14]	4.5×10^7 [15]	9.2×10^6 [16]	n/a	n/a	n/a
C_p	($J\,kg^{-1}\,K^{-1}$)	1.2×10^2 [17]	1.3×10^2	2.3×10^2 [18]	7.0×10^2	2.4×10^2	4.2×10^3
ρ	($kg\,m^{-3}$)	7.7×10^3	1.9×10^4	7.4×10^3	2.3×10^3	7.9×10^3	1.0×10^3
k	($W\,m^{-1}\,K^{-1}$)	1.3 [14]	3.2×10^2	58	1.6×10^2 [19]	10	0.59
S	($V\,K^{-1}$)	N, -2.3×10^{-4} [20] P, 2.1×10^{-4}	6.5×10^{-6}	1.2×10^{-6} [16]	n/a	n/a	n/a

to go from low to high field, is fixed at 5 ms for all switching frequencies. No distinction is made between the internal and the applied magnetic field with a strength of 1 T. Geometry specific influences like the demagnetizing field are neglected.

Of the experimental heat capacity measurements presented by Dan'kov [13], only the zero field ($H = 0$ T) data is used. Using a linearly interpolated heat capacity that varies with magnetic field strength, causes a discrepancy in the energy balance of the COMSOL Multiphysics model. For an adiabatic system, the magnetic work input is not completely reflected in the change in internal energy (calculated by integrating heat capacity over temperature). In other words, the heat capacity is fixed to 0 Tesla field strength, $C_p = C_p(0\,T,T)$, instead of $C_p = C_p(H,T)$. As a consequence, the adiabatic temperature step is slightly increased (≈3%), but this is deemed acceptable within the study scope. Negligible change is observed in the magnetic work input.

3.2. Peltier thermal diodes

The governing equations for the Peltier thermal diodes are respectively the energy and current conservation equation, coupled by the thermoelectric effect:

$$\rho C_p \frac{\partial T}{\partial t} + \vec{\nabla}\cdot(-k\vec{\nabla}T + P\vec{J}) = \vec{J}\cdot\vec{E} \tag{3}$$

$$\vec{\nabla}\cdot\vec{J} = \vec{\nabla}\cdot[-\sigma(\vec{\nabla}V + S\vec{\nabla}T)] = 0 \tag{4}$$

where the Peltier coefficient P is related to the Seebeck coefficient S by $P = ST$. The right-hand side of the energy equation is the Joule heat source where the electric field $\vec{E}$ is related to the electric potential V by $\vec{E} = -\vec{\nabla}V$. Each thermoelectric leg has a normal current density J_n in $A\,m^{-2}$ set on one side and a ground ($V = 0$) defined on the opposite end. The normal current density is related to the current by:

$$J_n = -\vec{n}\cdot\vec{J} = I/(d_z \cdot leg\ width) \tag{5}$$

Initially the current profiles are of the same shape as the magnetic field over time, only the cold side profile is shifted by half a period. The Peltier modules are most efficient at low electric power since the Peltier effect scales with the current and Joule heating is proportional to the current squared. The COP of the MPC-D701 module for $T_{hot} - T_{cold} = 0.1$ K near ambient temperature, is for Example 109 for 0.01 A, 53 for 0.02 A and 20 for 0.05 A.[3] In the model 0.01 A is used as an initial value. Additionally, a thermal contact conductance of $2 \times 10^5\ W\,m^{-2}\,K^{-1}$ (a value suggested by Micropelt) is assumed between the Peltier modules and the MCM.

[3] mypelt simulation tool (http://micropelt.com/products/mypelt.php), consulted on 18th of May 2016.

3.3. Heat exchangers

The heat exchangers are not uniform in z-direction (see Fig. 1a) and are therefore approximated in 2D (x,y-plane) by a porous medium. Kim [21] has demonstrated the validity of this method. Depending on the legitimacy of the local thermal equilibrium assumption, either a one-equation model or a two-equation model is applicable. Since the MCE is of relatively high power and only affects the solid, local thermal non-equilibrium is assumed and two energy equations are solved, coupled by a solid-fluid heat transfer term:

$$\theta_p \rho_s C_{p,s} \frac{\partial T_s}{\partial t} + \vec{\nabla}\cdot(-\theta_p k_s \vec{\nabla} T_s) = a_{sf} h_{sf} (T_f - T_s) \tag{6}$$

$$(1-\theta_p)\rho_f C_{p,f} \frac{\partial T_f}{\partial T} + (1-\theta_p)\rho_f C_{p,f} \vec{u}_f \cdot \vec{\nabla} T_f + \vec{\nabla}\cdot[-(1-\theta_p)k_f \times \vec{\nabla} T_f] = a_{sf} h_{sf} (T_s - T_f) \tag{7}$$

where a_{sf} is the amount of surface area per unit volume. The interstitial heat transfer coefficient h_{sf} in $W\,m^{-2}\,K^{-1}$ is calculated from the laminar Nusselt number correlation stated by Knight [22]:

$$Nu_{D_h} = -1.047 + 9.326G = \frac{h_{sf} D_h}{k_f} \tag{8}$$

where the parameter G is defined as:

$$G = \frac{(b/D)^2 + 1}{(b/D+1)^2} \tag{9}$$

and the hydraulic diameter D_h as:

$$D_h = \frac{2d_z}{N_{ch} + (w/b)(N_{ch} - 1) + (d_z/D)} \tag{10}$$

Here, b is the channel width, D the channel or fin height, w the channel wall or fin thickness and d_z the depth in z-direction (shown in Fig. 1a). The efficiency of the heat exchanger with respect to its height is estimated by considering the microchannel walls as fins and calculating the fin efficiency by:

$$\eta_{fin} = \frac{\tanh(mD)}{mD} \tag{11}$$

where:

$$m = \sqrt{\frac{2h_{sf}}{k_{fin} w}} \tag{12}$$

On the open inlet of a heat exchanger the temperature is set to a fixed value, on the outlet the temperature gradient is set to zero in normal direction ($\vec{n}\cdot\vec{\nabla}T = 0$). The heat exchangers are made of the same material (silicon) as the Peltier module substrate, therefore they could be made out of a single part without thermal contact resistance at the interface. The original microchannel velocity

$\vec{u}_f$ is converted to a porous medium velocity $\vec{u}_p$ via the solid volume fraction $\theta_p : \vec{u}_p = (1-\theta_p)\vec{u}_f$. The x-component of $\vec{u}_p$ is U in HHEX and $-U$ in CHEX, the y-component is 0 everywhere.

3.4. General method and output parameters

The system of equations above is solved by the PARDISO direct solver provided by COMSOL with a relative tolerance of 1×10^{-4}. A fully coupled scheme is used, which means T_f, T_s and V are solved simultaneously. For a fair comparison, all the simulations are run until periodic steady state is reached. This is verified by calculating the average enthalpy or temperature of the system. Further periods are not needed if the system state is nearly identical at the begin and end of a cycle.

The following expressions are evaluated to determine the device performance in periodic steady state. Starting with the temperature span which is determined by the difference in average fluid inlet temperature over a cycle:

$$T_{span} = \overline{T}_{f,c,in} - \overline{T}_{f,h,in} \tag{13}$$

The cooling power is determined by the fluid mass flow and load applied:

$$\dot{Q}_{c,load} = \dot{m} C_{p,f} \Delta T_{load} = \dot{m} C_{p,f} (\overline{T}_{f,h,in} - \overline{T}_{f,c,out}) \tag{14}$$

and the heating power by:

$$\dot{Q}_h = \dot{m} C_{p,f} (\overline{T}_{f,h,out} - \overline{T}_{f,c,in}) \tag{15}$$

The electric input power is calculated by summing the product of current and cycle average voltage difference over each leg:

$$P_{el} = \sum_{legs} (I \Delta \overline{V}_{leg}) \tag{16}$$

and the magnetic work input by:

$$\dot{W}_{mag} = \int_{V_{MCM}} \overline{\dot{Q}}_{MCE} \tag{17}$$

The COP based on cooling power is defined as:

$$COP_{cold} = \frac{\dot{Q}_{c,load}}{\dot{W}_{mag} + P_{el}} \tag{18}$$

Here, the pumping power is neglected since the velocity field is not solved for.

4. Results and discussion

Starting from an initial Peltier module and making alterations based on the performance characteristics, an approximation of the 3D geometry and the material properties is found. The result is converted to 2D and implemented in a single-stage device.

4.1. Final geometry

The MPC-D701 data sheet provides thermoelectric characteristics for several temperatures, in this study 25 °C is used as benchmark. By fixing the temperature on the bottom or top of the module, applying a small heat flux and solving the energy equation for solids, the thermal resistance can be estimated. The thermoelectric effect is not yet considered, so only the thermal conductivity of the materials used is of influence. In the final geometry, as shown in Fig. 3, no changes were made to the material properties. The available degrees of freedom to match the thermal resistance to the data sheet value (7.3 K W^{-1}) were: leg length (440 μm, z-dimension), leg width (41 μm, x-dimension) and the number of leg pairs in x-direction (19). Thermal resistance between the thin layers is neglected.

The maximum cooling power of the module is dependent on the balance between the Peltier effect transporting heat from cold to hot, Joule heating and thermal conduction. An optimum can be found since the Peltier effect scales linearly with current and Joule heating has a quadratic relationship. The choice was made to multiply the Seebeck coefficient of the thermoelectric materials by a factor (0.775) and alter the electrical contact resistance between the layers (2×10^{-11} Ωm^2, which is within the range mentioned by Böttner [11]) to match the maximum cooling power to the data sheet. These are sensible choices, since the bulk Seebeck coefficient is used and the actual coefficient is strongly dependent on the thin film production method, which also determines electrical contact resistance between the layers.

The resulting 2D computational domain for a single-stage device with mesh and boundary conditions is shown in Fig. 4. The Fourier number criterion, defined in Eq. (19), relates the thermal penetration depth to the mesh element size Δy. The solder and electrode layers are omitted so the large elements shown in y-direction can be used. This means that the electrical boundary conditions are directly imposed on the thermoelectric legs. A maximum solver time step of $\Delta t = 1 \times 10^{-5}$ s is sufficiently small to satisfy the Fourier number criterion. Table 2 summarizes the important properties.

$$Fo \equiv \frac{\alpha \Delta t}{\Delta y^2} = \frac{k \Delta t}{C_p \rho \Delta y^2} \ll 1 \tag{19}$$

4.2. (De)Magnetization and temperature step

Fig. 5 shows the average temperature of the magnetocaloric material for different configurations in periodic steady state. Here the heat exchangers are neglected and temperature boundary conditions are set on the interface of the heat exchangers with the upper ($T_{hot} = 293.4$ K) and lower ($T_{cold} = 293.15$ K) silicon substrate. The temperature difference of 0.25 K is based on the results of Section 4.3. The adiabatic MCM (Fig. 5a) shows the maximum temperature step, about 2.8 K, at a magnetic field change from 0 T (low temperature) to 1 T (high temperature), proportional to the shape of $H(t)$.

Fig. 5b depicts the temperature profile when a 100 μm thick sheet of MCM is integrated in a device with thermal diodes. The dashed lines indicate the behavior when both the thermal diodes stay passive (0 A). For the continuous lines, one of the Peltier modules is driven with a current of 0.01 A, as is described in Section 2.1. The initial temperature step after magnetization reduces to about 1 K, caused by the surrounding silicon being heated. Increasing the MCM thickness would bring the temperature step closer to the adiabatic case due to the thermal mass ratio shifting, but this would also yield a larger magnetized volume.

The default 525 μm substrate shows a pronounced, continued silicon heating effect: the 0.5 K drop in the ≈ 3 ms after magnetization. By reducing substrate thickness to 100 μm, as suggested by Böttner [11] and shown in Fig. 4, this effect is largely reduced. The temperature when the MCM and surrounding silicon have reached equilibrium, is the driving force for the heat flux to the hot and cold boundary in the passive case.

An applied current and resulting Peltier effect increases the heat extraction rate from the MCM. Some heat pumping is shown as well for the 100 μm case; after magnetization the temperature drops below T_{cold}. This behavior is not preferred since lattice conduction is now counteracting the Peltier effect. Fig. 6 gives a more in depth view of this behavior by showing the hot and cold boundary heat flux over time (a) and depicting the cross-sectional

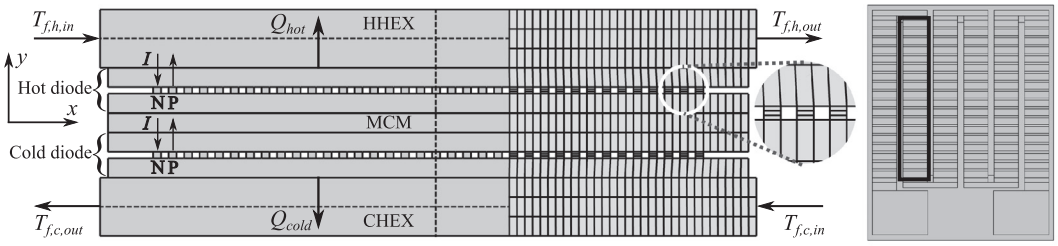

Fig. 4. 2D geometry, mesh and boundary conditions. The electric boundary conditions marked with an *I* are replicated over all the N- and P-type thermoelectric legs. The boundary heat fluxes Q_{cold} and Q_{hot} are depicted in Fig. 6a.

Table 2
2D geometry properties.

d_z	440 μm
W	3388 μm
MCM thickness	100 μm
Silicon thickness	100 μm
D	300 μm
N_{ch}	5
w	20 μm
b	64 μm
h_{sf}	2.9×10^4 W m^{-2} K
η_{fin}	64 %
θ_p	0.27
a_{sf}	2.8×10^5 m^{-1}

temperature profiles (b). The heat fluxes shown are positive in outward direction, so for a heat pumping effect the cold flux should be negative and the hot flux positive.

Just before magnetization the heat fluxes are almost symmetric, heat is pumped by the active Peltier module and the MCM is nearly passive. Magnetizing the MCM causes the desired hot side heating effect, but also parasitic heat leakage to the cold side, which is in the same order of magnitude. After demagnetization the same effect is seen, the MCM is heated nearly as much by the hot boundary as by the cold boundary.

Fig. 6b shows the temperature across the dashed vertical line of Fig. 4 for several key moments. Just before magnetization at 0.0475 s, the MCM is heated above T_{hot} by the active Peltier module on the cold side. During magnetization (0.05 s) the MCM temperature rises above the surrounding silicon and at the end of magnetization (0.0525 s) the MCM and silicon are at approximately the same temperature. Up to 0.0702 s both the temperature gradient and Peltier effect are transporting heat to the hot side, after that it is just the Peltier effect cooling the MCM to below T_{cold} until the start of demagnetization (0.1475 s). Based on this analysis, a higher frequency (20–25 Hz) is recommended to avoid superheating and subcooling by the Peltier modules. This has no influence on the parasitic heat fluxes after magnetization and demagnetization.

4.3. Temperature span with heat exchangers

Up to now the temperature difference between the hot and cold side has been fixed to 0.25 K. By including the heat exchangers in the simulation only one temperature needs to be defined. In this case the cold heat exchanger inlet temperature ($T_{f,c,in}$) is set to 293.15 K. The hot heat exchanger inlet temperature can be taken equal to the cold outlet (no load) or at some ΔT above the cold outlet (which translates to a load via the mass flow and heat capacity of water).

Fig. 7 shows the water temperature at the vertical center of the heat exchangers (dashed horizontal lines of Fig. 4), time averaged over a single cycle. For each line style, the upper line relates to HHEX and the lower line to CHEX. The vertical spacing between the temperatures is equal to the load at the left side and equal to the load plus system work input at the right side of the figure. With increasing load the slope decreases as there will be more heat leakage from the hot to the cold fluid.

The temperature gradient in *x*-direction is steeper for the cases at 0 T maximum field strength. This means that without the MCE and all heat pumping done by the Peltier modules, the heat pump reaches a larger temperature span at the same cooling load. The reason for this performance issue is the parasitic heat flux after (de)magnetization as seen in the fixed temperature span section. Several options for mitigating this effect are explored in Section 4.4.

The thermodynamic cycles are the same in 0 T and 1 T operations, just without the actual (de)magnetization or MCE. When operating at 0 T, the cold Peltier module is pumping heat to the

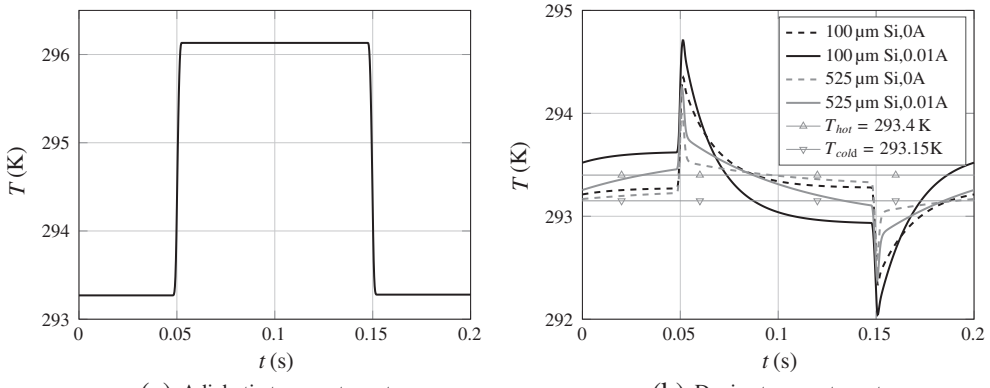

(a) Adiabatic temperature step (b) Device temperature step

Fig. 5. Magnetocaloric effect for different configurations at 5 Hz (τ_{cycle} = 0.2 s), note the difference in ordinate.

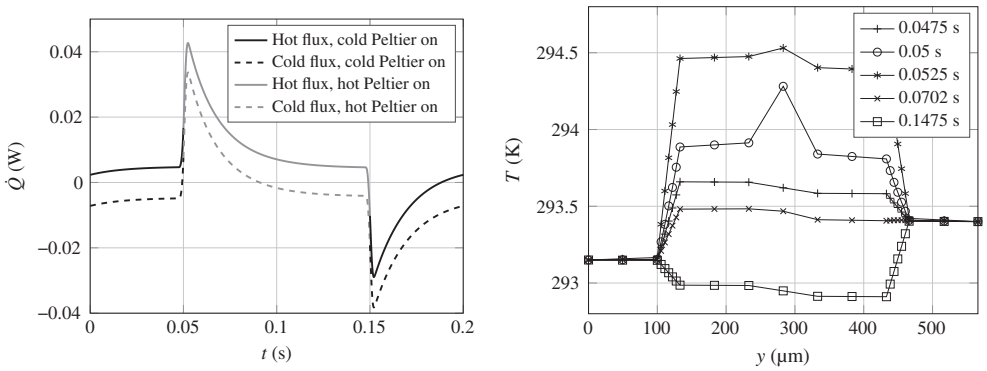

(a) Boundary heat flux as function of time. Magnetization and demagnetization with a duration of 5 ms are centered on $t = 0.05$ s and $t = 0.15$ s respectively.

(b) Vertical cross-section temperature

Fig. 6. Subcooling and superheating by the Peltier modules (5 Hz, 0.01 A, 100 μm MCM).

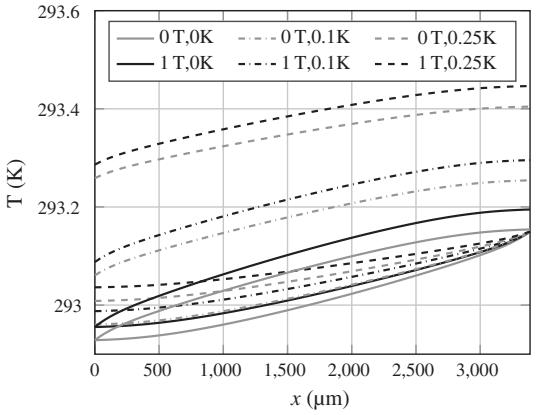

Fig. 7. Time averaged fluid temperatures (20 Hz, 0.01 A, 100 μm MCM, 0.05 m s^{-1} fluid velocity).

MCM and the hot Peltier module pumps that heat to HHEX. The operation of both Peltier modules is still sequential.

Performance characteristics for several load cases are displayed in Table 3. For every parameter permutation the following relation holds: $\dot{Q}_h = \dot{Q}_{c,load} + P_{el} + \dot{W}_{mag}$ (up to a rounding error). The negative cooling power for 0 K load is the temperature boundary condition at HHEX inlet, allowing the fluid to conduct heat ($\vec{n} \cdot \vec{\nabla} T \neq 0$). As it is expected, the temperature span decreases with increasing load and even becomes negative ($T_{f,c,in} > T_{f,h,in}$) for 0.25 K load. The COP is an order of magnitude larger for all loads without the MCE. This is due to the magnetic work input also being about 10 times as large as the electric power. Increasing fluid velocity reduces temperature span but doubles the cooling power.

The usable temperature span of a single device, as shown in Table 3, is calculated by taking the difference between cold and hot inlet. Divided by the length, this becomes a temperature gradient in K m^{-1}. To investigate if this relation holds for larger geometries, 10 devices in series are simulated. For the combined single-stages, resulting in an AMR, only the heat exchangers are in contact. The thermal diodes and MCM are isolated from each other in x-direction to avoid excessive longitudinal heat conduction. This is assured by a gap in the geometry and assuming adiabatic walls. Fig. 8 shows the time averaged temperature profiles for several cases. Similar to the single device, the upper line of a line style relates to HHEX and the lower line to CHEX.

At 0.25 K load and 0.05 m s^{-1} the cold fluid is first heated and then cooled. The work input by Joule heating and the magnetocaloric effect can only leave the system via the hot outlet. This means that heat accumulates in the hot fluid, raising its temperature and reaching a maximum near the cold inlet. Due to the low thermal resistance of the Peltier modules, enough heat leaks to the cold fluid to counteract all heat pumping and even raise its temperature. Integrating the cold side heat flux (downward positive) over 1 period for the leftmost (−3.17 J) and rightmost stage (0.64 J) proves this statement. Using a higher velocity (0.1 m s^{-1}) increases fluid heat transport capacity, hence the hot fluid outlet temperature is reduced and the cold fluid is no longer heated. Based on the cold fluid outlet temperature at 0.25 K load, the single-stage device has a temperature gradient of 34 K m^{-1} and for 10 repetitions this reduces to 14 K m^{-1}. Build-up of heat leakage in the cold fluid significantly reduces scalability. The temperature gradient without the MCE is 42 K m^{-1} for the single-stage device and 39 K m^{-1} for 10 repetitions, so both a larger temperature span and better scaling is observed.

Table 3
Performance data for several parameter variations at 20 Hz, 0.01 A, 100 μm MCM.

H_{max} (T)	ΔT_{load} (K)	U (m s^{-1})	T_{span} (K)	$\dot{Q}_{c,load}$ (mW)	$\dot{Q}_h$ (mW)	P_{el} (mW)	$\dot{W}_{mag}$ (mW)	$COP_{cooling}$
0	0	0.05	0.22	−0.020	0.098	0.119	0	n/a
1	0	0.05	0.19	−0.021	1.224	0.100	1.147	n/a
0	0.1	0.05	0.09	2.747	2.866	0.121	0	23.7
1	0.1	0.05	0.06	2.746	4.008	0.102	1.161	2.2
0	0.25	0.05	−0.11	6.896	7.020	0.124	0	55.6
1	0.25	0.05	−0.14	6.894	8.182	0.105	1.183	5.4
0	0.1	0.1	0.00	5.523	5.642	0.120	0	46.0
1	0.1	0.1	−0.01	5.522	6.788	0.101	1.166	4.4

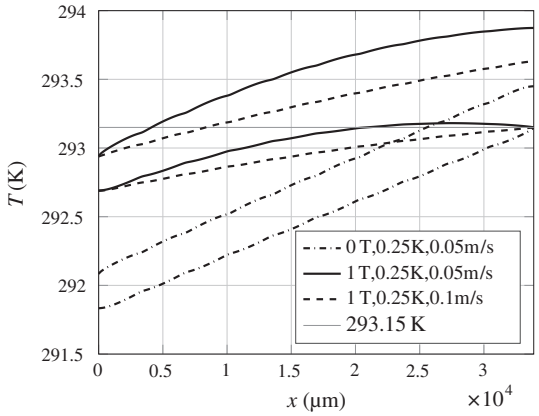

Fig. 8. Time averaged fluid temperatures for 10 stages in series (20 Hz, 0.01 A, 100 μm MCM).

4.4. Parasitic heat flux mitigation

The unmodified device has shown better performance by disabling the magnetocaloric effect and solely relying on the heat pumping done by the Peltier modules. The aim of this section is to investigate if it is possible to modify the single-stage device in such a way that the magnetocaloric effect can be successfully employed. Initially the modification considers changing operational parameters, followed by altering the geometry of the device.

4.4.1. Active countermeasure: always on

In theory, negligible leakage of heat to the cold fluid would result in a better temperature span. This can be achieved by simultaneously driving a current through both diodes, such that the hot module extracts heat and the cold module counteracts parasitic heat flux or vice versa. In other words, both modules are always on, driven by a constant current.

At a current of 0.01 A, near zero net heat flux is achieved in the period between magnetization and demagnetization, as shown in Fig. 9a. The heat flux without the MCE (Fig. 9b) is a flat line; no periodic behavior is seen. The improvement made is equal to the difference with the original heat flux profile. The temperature span, presented in Table 4, is increased significantly with and without the MCE. The cost is more than double the electric power input. The COP for $H_{max} = 0$ T is therefore reduced by 50 %. Interestingly, the COP with a magnetic field increases by about 20%. This is due to the temperature dependence of the MCE. Compared to the original case, the average MCM temperature is significantly lower for the case where the thermal diodes are always on. This modification does improve temperature span, but still better performance is seen without the MCE.

4.4.2. Change in geometry: thicker layer of thermoelectric material

A passive way of improving device performance is found by increasing thermal diode resistance. This is achieved by using a thicker layer of highly insulating thermoelectric material (Bi_2Te_3). The original layer is increased from 33 μm to 50 μm and 100 μm thickness. The resulting heat flux profiles with and without the MCE are shown in Fig. 9a and b respectively. The peak in heat leakage after magnetization at 0.0125 s reduces significantly with thicker thermoelectric material. Without the MCE, the same behavior is seen to a lesser extent.

As it is expected, the temperature span improves with this modification, as reported in Table 4. On the downside, the electric input power and resulting amount of Joule heating are more than the original due to the longer current path. Therefore, the COP for $H_{max} = 0$ T reduces with increasing layer thickness. The COP with the MCE enabled remains nearly constant, since the extra electric power is compensated by a drop in the temperature dependent magnetic work input. Similar to the active modification, performance improvement is observed but the case without the MCE is not surpassed by the case with the MCE enabled.

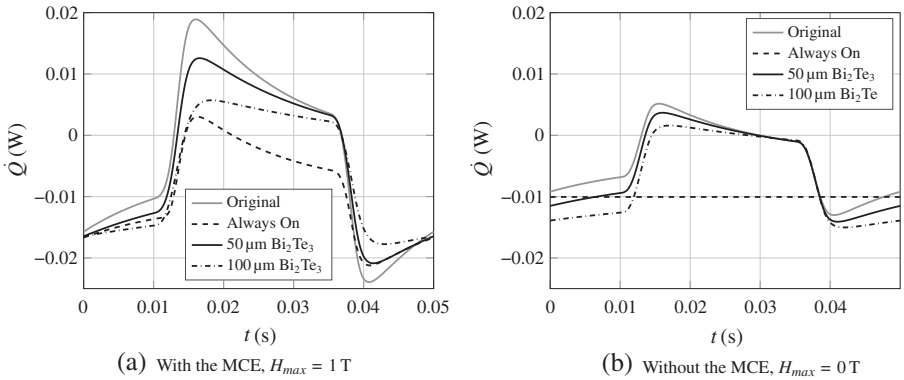

(a) With the MCE, H_{max} = 1 T (b) Without the MCE, H_{max} = 0 T

Fig. 9. Cold boundary heat flux of the original and the modifications explored (0.25 K load, 20 Hz, 0.05 m s^{-1}).

Table 4
Performance data of the original and the modifications explored (0.25 K load, 20 Hz, 0.05 m s^{-1}).

Case	T_{span} (K)	$\dot{Q}_{c,load}$ (mW)	$\dot{Q}_h$ (mW)	P_{el} (mW)	$\dot{W}_{mag}$ (mW)	$COP_{cooling}$
Original, 0 T	−0.11	6.896	7.020	0.124	0	55.6
Original, 1 T	−0.14	6.894	8.182	0.105	1.183	5.4
Always on, 0 T	0.11	6.877	7.137	0.260	0	26.5
Always on, 1 T	0.09	6.876	7.928	0.260	0.794	6.5
50 μm Bi_2Te_3, 0 T	−0.06	6.892	7.071	0.180	0	38.3
50 μm Bi_2Te_3, 1 T	−0.09	6.891	8.153	0.158	1.104	5.5
100 μm Bi_2Te_3, 0 T	−0.01	6.888	7.231	0.342	0	20.1
100 μm Bi_2Te_3, 1 T	−0.03	6.886	8.188	0.318	0.984	5.3

5. Conclusion and recommendations

Contrary to the work published by Tomc and others, this article shows a less optimistic outlook on application of thermoelectric thermal diodes in a magnetocaloric heat pump. The expected improvement in operation frequency and therefore power density is observed, but this happens in conjunction with an unwanted side effect. Heat leaking through the passive thermal diode causes a reduction in the temperature span when comparing configurations with and without the MCE enabled. In other words, a heat pump solely based on the Peltier effect shows better performance than one employing both the MCE and the Peltier effect. Next to a slightly larger temperature span, the COP differs by an order of magnitude caused by the absence of magnetic work input.

The above statement is based on purely numerical work with numerous assumptions, so the first and foremost recommendation is to validate if this conclusion also holds experimentally. The numerical model itself can be improved by incorporating a thermodynamically sound implementation of the magnetocaloric effect based on the mean field theory. The power density at a realistic temperature span (e.g. a household fridge) can be determined by increasing the number of devices in series and investing more computational time.

Thermal diodes of some form are essential for successful commercialization of magnetocaloric refrigeration. Based on the results of this article, Peltier thermal diodes (i.e. Micropelt MPC-D701) have lost some of their potential. Thermal switches employing geometric isolation, by for example electrowetting, might be a promising alternative (Cha [23]).

References

[1] A. Kitanovski, J. Tušek, U. Tomc, U. Plaznik, M. Ozbolt, A. Poredoš, Magnetocaloric Energy Conversion, Springer, 2015, http://dx.doi.org/10.1007/978-3-319-08741-2.

[2] A. Kitanovski, P.W. Egolf, Innovative ideas for future research on magnetocaloric technologies, Int. J. Refrig. 33 (3) (2010) 449–464, http://dx.doi.org/10.1016/j.ijrefrig.2009.11.005.

[3] D. Silva, B. Bordalo, A. Pereira, J. Ventura, J. Araújo, Solid state magnetic refrigerator, Appl. Energy 93 (2012) 570–574, http://dx.doi.org/10.1016/j.apenergy.2011.12.002.

[4] D.J. Silva, J. Ventura, J.P. Araújo, A.M. Pereira, Maximizing the temperature span of a solid state active magnetic regenerative refrigerator, Appl. Energy 113 (2014) 1149–1154, http://dx.doi.org/10.1016/j.apenergy.2013.08.070.

[5] U. Olsen, C. Bahl, K. Engelbrecht, K. Nielsen, Y. Tasaki, H. Takahashi, Modeling of in-vehicle magnetic refrigeration, Int. J. Refrig. 37 (2014) 194–200, http://dx.doi.org/10.1016/j.ijrefrig.2013.09.013.

[6] U. Tomc, J. Tušek, A. Kitanovski, A. Poredoš, A new magnetocaloric refrigeration principle with solid-state thermoelectric thermal diodes, Appl. Therm. Eng. 58 (1-2) (2013) 1–10, http://dx.doi.org/10.1016/j.applthermaleng.2013.03.063.

[7] U. Tomc, J. Tušek, A. Kitanovski, A. Poredoš, A numerical comparison of a parallel-plate AMR and a magnetocaloric device with embodied micro thermoelectric thermal diodes, Int. J. Refrig. 37 (1) (2014) 185–193, http://dx.doi.org/10.1016/j.ijrefrig.2013.07.003.

[8] P.W. Egolf, L. Gravier, T. Francfort, a.G. Pawlowski, G. Courret, M. Croci, High-frequency magnetocaloric modules with heat gates operating with the Peltier effect, Int. J. Refrig. 37 (1) (2014) 176–184, http://dx.doi.org/10.1016/j.ijrefrig.2013.09.028.

[9] MicroPelt GmbH, MPC-D701 Datasheet. <http://www.micropelt.com/down/datasheet_mpc_d701.pdf>.

[10] H. Böttner, J. Nurnus, A. Gavrikov, G. Kühner, M. Jägle, C. Künzel, D. Eberhard, G. Plescher, A. Schubert, K.H. Schlereth, New thermoelectric components using microsystems technologies, J. Microelectromech. Syst. 13 (3) (2004) 414–420, http://dx.doi.org/10.1109/JMEMS.2004.828740.

[11] H. Böttner, Micropelt miniaturized thermoelectric devices: Small size, high cooling power densities, short response time, in: International Conference on Thermoelectrics, ICT, Proceedings 2005, 2005, pp. 1–8, http://dx.doi.org/10.1109/ICT.2005.1519873.

[12] H. Böttner, J. Nurnus, A. Schubert, F. Volkert, New high density micro structured thermogenerators for stand alone sensor systems, in: International Conference on Thermoelectrics, ICT, Proceedings, 2007, pp. 306–309, http://dx.doi.org/10.1109/ICT.2007.4569484.

[13] S.Y. Dan'kov, A.M. Tishin, V. Pecharsky, K. Gschneidner, Magnetic phase transitions and the magnetothermal properties of gadolinium, Phys. Rev. B 57 (6) (1998) 3478–3490, http://dx.doi.org/10.1103/PhysRevB.57.3478.

[14] L.M. Goncalves, C. Couto, P. Alpuim, A.G. Rolo, F. Völklein, J.H. Correia, Optimization of thermoelectric properties on Bi2Te3 thin films deposited by thermal co-evaporation, Thin Solid Films 518 (10) (2010) 2816–2821, http://dx.doi.org/10.1016/j.tsf.2009.08.038.

[15] D.R. Lide, Handbook of Chemistry and Physics, seventy fifth ed., CRC Press, New York, 1996. <http://hypertextbook.com/facts/2004/JennelleBaptiste.shtml>.

[16] S. Mhiaoui, Physical properties of lead free solders in liquid and solid state (Ph. D. thesis), Chemnitz University of Technology, 2007. <http://www.qucosa.de/fileadmin/data/qucosa/documents/5563/data/Dissertation_Mhiaoui.pdf>.

[17] N. Gorbachuk, V. Sidorko, Heat capacity and enthalpy of Bi2Si3 and Bi2Te3 in the temperature range 58–1012 K, Powder Metall. Met. Ceram. 43 (437) (2004) 284–290, http://dx.doi.org/10.1023/B:PMMC.0000042464.28118.a3.

[18] Y.K. Wu, K.L. Lin, B. Salam, Specific heat capacities of Sn-Zn-based solders and Sn-Ag-Cu solders measured using differential scanning calorimetry, J. Electron. Mater. 38 (2) (2008) 227–230, http://dx.doi.org/10.1007/s11664-008-0589-y.

[19] C.J. Glassbrenner, G.A. Slack, Thermal conductivity of silicon and germanium from 3 K to the melting point, Phys. Rev. 134 (4A). doi:http://dx.doi.org/10.1103/PhysRev.134.A1058.

[20] N.D. Lowhorn, W. Wong-Ng, Z.Q. Lu, E. Thomas, M. Otani, M. Green, N. Dilley, J. Sharp, T.N. Tran, Development of a seebeck coefficient standard reference material, Appl. Phys. A 96 (2) (2009) 511–514, http://dx.doi.org/10.1007/s00339-009-5191-5.

[21] S. Kim, D. Kim, D. Lee, On the local thermal equilibrium in microchannel heat sinks, Int. J. Heat Mass Transfer 43 (10) (2000) 1735–1748, http://dx.doi.org/10.1016/S0017-9310(99)00259-8.

[22] R. Knight, D. Hall, J. Goodling, R. Jaeger, Heat sink optimization with application to microchannels, IEEE Trans. Compon. Hybr. Manuf. Technol. 15 (5) (1992) 832–842, http://dx.doi.org/10.1109/33.180049.

[23] G. Cha, C.J. Kim, Y.S. Ju, Thermal conductance switching based on the actuation of liquid droplets through the electrowetting on dielectric (EWOD) phenomenon, Appl. Therm. Eng. 98 (2016) 189–195, http://dx.doi.org/10.1016/j.applthermaleng.2015.11.098.